Vibrational power flow analysis of cracked functionally graded beams

Lin-Feng Zhu [a], Liao-Liang Ke [a,b*], Yang Xiang [c], Xin-Qun Zhu [d], Yue-Sheng Wang [b]

[a] *Institute of Engineering Mechanics, Beijing Jiaotong University, Beijing, 100044, China*

[b] *School of Mechanical Engineering, Tianjin University, Tianjin, 300350, China*

[c] *School of Engineering, Western Sydney University, Penrith, NSW 2751, Australia*

[d] *School of Civil and Environmental Engineering, University of Technology Sydney, Broadway NSW 2007, Australia*

Abstract.

In this paper, the vibrational power flow of a cracked beam made of functionally graded materials (FGMs) is investigated. The Young's modulus and mass density change exponentially along the thickness direction of the beam. The cracked FGM beam is divided into two sub-beams at the crack section which are connected by a massless rotational spring. Based on the Timoshenko beam theory, the governing equations of the cracked FGM beam are derived by using the neutral plane as the reference plane. The dynamic response of the FGM beam subjected to a harmonic concentrated transverse force is solved by the wave propagation approach. The input power flow and the transmitted power flow are obtained. The effect of the crack location and depth and the Young's modulus ratio on the input power flow and the transmitted power flow is studied in detail. A new damage index (DI) for the crack identification of FGM beams is proposed by applying continuous wavelet transform (CWT) to the transmitted power flow distribution along the beam longitudinal direction. The peak of DI indicates the crack location in FGM beams with small crack depth.

Keywords: Functionally graded beam; Vibrational power flow; Edge crack; Damage identification; Continuous wavelet transform

*Corresponding author. Tel.: 86-10-51685755

E-mail address: llke@bjtu.edu.cn, llke@tju.edu.cn (Liao-Liang Ke)

1. Introduction

Structures in engineering applications are always subjected to dynamic forces from external load and internal operation of machines, which may result in structural damage and high level of structure-borne noises. Hence, it is important to assess and minimize vibrational energy level of structures. The vibrational power flow is a time-averaged quantity which combines the effects of both forces and velocities. It is desirable to identify the magnitude and transmission path of the vibrational energy in structures in order to prevent damage and reduce the noise level of structures. Early studies of power flows in structures can be traced back to five decades ago [1-3]. In 1980, Goyder and White [4-6] introduced the expression of the structural power flow when force and velocity were harmonic. They studied the power flow of infinite beam and plate, stiffened plate and isolation system. Bouthier and Bernhard [7] derived the power balance equation in plates based on the local space averaged energy flow. This energy flow model as a new approach was used generally for high frequency response analysis of structures [8]. Chen and Wang [9] performed wave attenuation and power flow analysis of sandwich beams with internal absorbers. They found that the power flow of the sandwich beam reduces with the greater extent of attenuation of the flexural wave. Liu et al. [10] studied propagation characteristics of the vibrational power flow in a laminated composite cylindrical shell filled with fluid. At present, the power flow analysis becomes an important tool for studying the structural noise [11], isolation system [12], power transmission [13], etc.

In 1990s, a new type of composite materials that characterizes by continuous spatial change in constituent materials and material properties was introduced to resist high thermal stress, named the functionally graded materials (FGMs) [14]. With the extension of the concept of gradient and the development of fabrication technology [15], material scientists developed various FGM systems with different combinations of constituent materials, bi-directional FGMs, structures with graded geometrical parameter [16,17]. Because of their excellent thermo-mechanical performance, FGMs are implemented in a wide range of fields such as aerospace, marine engineering, mechanical engineering, biomaterials, energy, etc. FGM beams are used as the key parts in these applications, such as the turbine blade, cutting-tool, marine propeller, actuator, etc.

For an FGM beam with inhomogeneous material properties, the neutral plane of the beam may differ from the geometric midplane of the beam [18]. The governing equations based on the physical neutral plane have similar forms as those of homogeneous beams due to the elimination of the bending-stretching coupling [19]. By using the neutral plane model, many researches on the dynamic behavior of FGM beams

were conducted [18, 20-25]. However, studies on the power flow of FGM structures are scarce. Liu and Niu [26] proposed an energy flow model for FGM beams to obtain structural energy density distributions, which had good correlation and accuracy in comparison with that by mode superposition.

It is well known that crack and damage inevitably exist in structures. The occurrence of crack and damage will change the dynamic characteristics of structures. The equivalent line spring model is widely employed to replace the crack in structural dynamic analysis. Li et al. [27] studied the power flow of periodically simply supported beam with cracks using the transfer matrix approach. The beam is divided into two segments connected by the rotational spring at the crack section. Then, they investigated the input power flow and transmitted power flow of intact and damaged beams with infinite length [28]. They found that the occurrence of cracks has significant influence on the vibrational power flow of the beams. Zhu et al. [29] further proposed a crack identification method based on contours of changes of the input power flow. This approach was extended to the crack identification of the thin cylindrical shell with a circumferential surface crack [30] and the plate with a part-through surface crack [31].

In comparison with the method based on the input power flow [29-31], the spatial distribution of the transmitted power flow indicates the transmission of energy in structures and provides more local information. The continuous wavelet transform (CWT) as a signal processing tool is widely employed in the damage identification due to its very high sensitivity to the local singularity of tested signals [32]. The data of spatially distributed response from the damaged structures carried local singularity at damage location, such as static deflection [33], the mode shape [34], the operational deflection shapes [35] and the active thermography [36], can be treated as tested signals and transformed into a series of wavelet coefficients by CWT. The information of damage can be obtained from the peak of wavelet coefficients. The spatial distribution of the transmitted power flow captures the clear peak at the crack location, especially for the greater crack depth. Therefore, we can apply CWT of the transmitted power flow for the crack identification.

This paper investigates the vibrational power flow of cracked FGM beams under a concentrated transverse harmonic force by using the rotational spring model. The beam is divided into two sub-beams at the crack section connected by a massless rotational spring which is equivalent to the crack. Based on the Timoshenko beam theory, the governing equations of the cracked FGM beam are derived, and then solved to obtain the input power flow and transmitted power flow by using the wave propagation approach. The effect of the crack location, the crack depth and the Young's modulus ratio on the power flow is discussed.

By applying continuous wavelet transform (CWT) to the transmitted power flow distribution, a new crack identification method is developed for cracked FGM beams.

2. Linear rotational spring model

Fig. 1a shows an infinite FGM beam with an open edge crack of depth *a* located at L_1 to the right side of the driving source. The thickness of the beam is *h*. The coordinate *z* is with respect to the geometric middle plane of the beam ($z = 0$). The Young's modulus $E(z)$ and mass density $\rho(z)$ of the beam are assumed to change with exponential function along the z-axes direction, i.e.

$$E(z) = E_m e^{\beta z}, \rho(z) = \rho_m e^{\beta z}, \tag{1}$$

where $\beta = \ln(E_2 / E_1)/h$ is the gradient index; E_1 and E_2 represent the elastic modulus of the top and bottom surfaces of the beam, respectively; E_m and ρ_m are the Young's modulus and the mass density at the middle plane, respectively. The Poisson's ratio μ is taken to be a constant.

As the material properties of an FGM beam may be non-symmetric about the coordinate axes *z*, the neutral plane of the beam can be different from the geometric midplane of the beam. The position of the neutral plane z_0 of the beam is determined by [18]

$$z_0 = \frac{\int_{-h/2}^{h/2} \frac{E(z)}{1-\mu^2} z \mathrm{dz}}{\int_{-h/2}^{h/2} \frac{E(z)}{1-\mu^2} \mathrm{dz}}. \tag{2}$$

In Fig. 1b, a massless rotational spring is employed to simulate the open edge crack. The FGM beam is split into two separated sub-beams connected by a rotational spring at the crack location. In the rotational spring model, only the discontinuity of the bending slop at the crack section is considered. This model will be used in the vibrational power flow analysis of FGM beam. The bending stiffness K_T of the spring can be given as

$$K_T = \frac{1}{G}, \tag{3}$$

where *G* is the flexibility. At the cracked location, it can be expressed as [37]

$$\frac{\left(1-\mu^2\right)K_1^2}{E(a)}=\frac{M^2}{2}\frac{\mathrm{d}G}{\mathrm{d}a}, \tag{4}$$

where M is the bending moment at the crack location; K_1 is the stress intensity factor (SIF) under the mode I bending load; $E(a)$ is the Young's modulus at the crack tip.

Based on the values of the mode I SIF of the FGM strip given by Erdogan and Wu [38], the relationship between K_1 and the crack depth ratio ξ can be given by the Lagrange interpolation method [39]:

$$K_1=\frac{6M\sqrt{\pi h\xi}}{h^2}\Phi(\xi),\ \ \xi=\frac{a}{h},\ \ \xi\le 0.7, \tag{5}$$

where the range of crack depth ratio is from 0 to 0.7. $\Phi\left(\xi\right)$ is given as

$$\begin{aligned}E_2/E_1=0.2:\ \Phi\left(\xi\right)=&1.910-2.752\xi-4.742\xi^2+146.776\xi^3-770.750\xi^4\\&+1947.830\xi^5-2409.170\xi^6+1177.980\xi^7,\end{aligned} \tag{6a}$$

$$\begin{aligned}E_2/E_1=1:\ \Phi\left(\xi\right)=&1.150-1.662\xi+21.667\xi^2-192.451\xi^3+909.375\xi^4\\&-2124.310\xi^5+2395.830\xi^6-1031.750\xi^7,\end{aligned} \tag{6b}$$

$$\begin{aligned}E_2/E_1=5:\ \Phi\left(\xi\right)=&0.650-0.859\xi+12.511\xi^2-72.627\xi^3+267.910\xi^4\\&-535.236\xi^5+545.139\xi^6-211.706\xi^7.\end{aligned} \tag{6c}$$

Substitution of Eq. (5) into Eq. (4) leads to

$$\mathrm{G}=\int_0^{\xi}\frac{72\pi\left(1-\mu^2\right)\xi\Phi^2\left(\xi\right)}{E\left(\xi h\right)h^2}\mathrm{d}\xi. \tag{7}$$

Then, the bending stiffness of the rotational spring at the crack section can be determined from Eqs. (3) and (7).

Note that it is inevitable to occur the stress concentration at the crack tip when the harmonic force is applied to the cracked beam. This stress concentration will yield the materials and leads to the plastic area around the crack tip. In the present analysis, we assume that the plastic area at the crack tip is small and its effect is negligible.

3. Formulations of cracked FGM Timoshenko beam

Based on the Timoshenko beam theory, the axial displacement $\bar{u}(x,z,t)$ and transverse

displacement $\overline{w}(x,z,t)$ are respectively written as

$$\overline{u}(x,z,t) = (z - z_0)\psi(x,t), \tag{8}$$

$$\overline{w}(x,z,t) = w(x,t), \tag{9}$$

where z_0 is the position of the neutral plane; t is time; $w(x,t)$ is the transverse displacement at the middle plane; and $\psi(x,t)$ is the rotation of the cross section.

The normal stress and shear stress are respectively given by

$$\sigma_{xx} = \frac{E(z)}{1-\mu^2}(z - z_0)\frac{\partial \psi}{\partial x}, \tag{10}$$

$$\tau_{xz} = \frac{E(z)}{2(1+\mu)}(\frac{\partial w}{\partial x} + \psi). \tag{11}$$

The bending moment and transverse shear force are

$$M = \int\int_A \sigma_{xx}(z - z_0)\mathrm{dA} = D_{11}\frac{\partial \psi}{\partial x}, \tag{12}$$

$$Q = \kappa\iint_A \tau_{xz}\mathrm{dA} = \kappa A_{55}(\frac{\partial w}{\partial x} + \psi), \tag{13}$$

where κ is the shear correction factor which is related to the Poisson's ratio and shape of the cross section. For a beam with a rectangular cross section, it is reasonable for κ to take the value of 5/6. The stiffness components are defined as

$$D_{11} = \int_{-h/2}^{h/2}\frac{E(z)}{1-\mu^2}(z - z_0)^2\mathrm{dz}, \tag{14}$$

$$A_{55} = \int_{-h/2}^{h/2}\frac{E(z)}{2(1+\mu)}\mathrm{dz}. \tag{15}$$

By using the Hamilton principle, the governing equation of cracked FGM beams can be obtained by

$$\kappa A_{55}\left(\frac{\partial^2 w_j}{\partial x^2} + \frac{\partial \psi_j}{\partial x}\right) = I_1\frac{\partial^2 w_j}{\partial t^2}, \tag{16}$$

$$D_{11}\frac{\partial^2 \psi_j}{\partial x^2} - \kappa A_{55}\left(\frac{\partial w_j}{\partial x} + \psi_j\right) = I_3\frac{\partial^2 \psi_j}{\partial t^2}, \tag{17}$$

where the subscript j = 1, 2 denotes the left sub-beam and right sub-beam; I_1 and I_3 are the inertia terms

$$\{I_1, I_3\} = \int_{-h/2}^{h/2} \rho(z)\{1, (z-z_0)^2\}\mathrm{d}z. \tag{18}$$

Meanwhile, the compatibility conditions at the crack location $x = L_1$ require

$$W_1(L_1) = W_2(L_1), \quad K_T\left[\Psi_2(L_1) - \Psi_1(L_1)\right] = M_1(L_1), \quad M_1(L_1) = M_2(L_1), \quad Q_1(L_1) = Q_2(L_1). \tag{19}$$

For a beam in harmonic vibration, the solutions of transverse displacement and rotation of the beam can be written as

$$\psi_j(x,t) = \Psi_j(x)\mathrm{e}^{\mathrm{i}\omega t}, \tag{20}$$

$$w_j(x,t) = W_j(x)\mathrm{e}^{\mathrm{i}\omega t}, \tag{21}$$

where $\mathrm{i} = \sqrt{-1}$; ω is the angular frequency.

Substituting Eqs. (20)-(21) into Eqs. (16)-(17), the governing equations can be rewritten as

$$\frac{\mathrm{d}^4\Psi_j}{\mathrm{d}x^4} + (m+n)\frac{\mathrm{d}^2\Psi_j}{\mathrm{d}x^2} + (mn-p)\Psi_j = 0, \tag{22}$$

$$\frac{\mathrm{d}^4 W_j}{\mathrm{d}x^4} + (m+n)\frac{\mathrm{d}^2 W_j}{\mathrm{d}x^2} + (mn-p)W_j = 0, \tag{23}$$

where m, n and p are denoted as

$$m = \frac{I_1\omega^2}{\kappa A_{55}}, \quad n = \frac{I_3\omega^2}{D_{11}}, \quad p = \frac{I_1\omega^2}{D_{11}}. \tag{24}$$

The solutions of Eqs. (22) and (23) are expressed as

$$W_j(x) = f_{1j}\mathrm{e}^{-k_1 x} + f_{2j}\mathrm{e}^{k_1 x} + f_{3j}\mathrm{e}^{-\mathrm{i}k_2 x} + f_{4j}\mathrm{e}^{\mathrm{i}k_2 x}, \tag{25}$$

$$\Psi_j(x) = q_1 f_{1j}\mathrm{e}^{-k_1 x} - q_1 f_{2j}\mathrm{e}^{k_1 x} - q_2 f_{3j}\mathrm{e}^{-\mathrm{i}k_2 x} + q_2 f_{4j}\mathrm{e}^{\mathrm{i}k_2 x}, \tag{26}$$

where

$$k_1 = \sqrt{\sqrt{\left(\frac{m-n}{2}\right)^2 + p} - \frac{m+n}{2}}, \quad k_2 = \sqrt{\sqrt{\left(\frac{m-n}{2}\right)^2 + p} + \frac{m+n}{2}}, \tag{27a}$$

$$q_1 = \frac{k_1^2 + m}{k_1}, \quad q_2 = \frac{k_2^2 - m}{\mathrm{i}k_2}. \tag{27b}$$

The unknown constants f_{1j}, f_{2j}, f_{3j} and f_{4j} can be solved from the conditions at the driving source and crack location.

According to Eqs. (25), (26) and (27a), there is a critical frequency ω_c determining whether the

waves with wavenumber k_1 are propagating or evanescent. For FGM beams, the critical frequency can be expressed as

$$\omega_c = \sqrt{\frac{\kappa A_{55}}{I_3}}\,. \tag{28}$$

When $\omega > \omega_c$, two kinds of waves propagate with wavenumbers k_1 and k_2, respectively; when $\omega \le \omega_c$, only the waves with wavenumber k_1 propagates. In the present analysis, the driving frequency is far below the critical frequency.

4. Solutions of intact FGM beams

For an infinite intact FGM beam under a concentrated harmonic force $F_0 \mathrm{e}^{\mathrm{i}\omega t}$ at $x = 0$, there are four forced waves away from the driving source, as shown in Fig. 2a. Then, the intact FGM beam is divided into two sub-beams at the driving source, and the transverse displacement and rotation can be written as,

$$\begin{pmatrix} W_1(x) \\ \Psi_1(x) \end{pmatrix} = \begin{pmatrix} f_{21} & f_{41} \\ -q_1 f_{21} & q_2 f_{41} \end{pmatrix} \begin{pmatrix} \mathrm{e}^{k_1 x} \\ \mathrm{e}^{\mathrm{i}k_2 x} \end{pmatrix}, \tag{29}$$

for $x \le 0$,

$$\begin{pmatrix} W_2(x) \\ \Psi_2(x) \end{pmatrix} = \begin{pmatrix} f_{12} & f_{32} \\ q_1 f_{12} & -q_2 f_{32} \end{pmatrix} \begin{pmatrix} \mathrm{e}^{-k_1 x} \\ \mathrm{e}^{-\mathrm{i}k_2 x} \end{pmatrix}, \tag{30}$$

for $x \ge 0$, where the subscripts “1” and “2” denote the components related to the negative and the positive directions from the driving source, respectively. For the intact FGM beam, the continuity conditions at the driving point $x = 0$ can be expressed as

$$W_1(0) = W_2(0), \quad \Psi_1(0) = \Psi_2(0), \quad M_1(0) = M_2(0), \quad Q_1(0) = -Q_2(0) = \frac{F_0}{2}. \tag{31}$$

Substituting Eqs. (29) and (30) into Eq. (31), the four unknowns are obtained by utilizing the four continuity conditions in Eq. (31):

$$f_{21} = f_{12} = \frac{q_2 F_0}{2\kappa A_{55}(k_1 q_2 + \mathrm{i}k_2 q_1)}, \quad f_{41} = f_{32} = \frac{q_1 F_0}{2\kappa A_{55}(k_1 q_2 + \mathrm{i}k_2 q_1)}. \tag{32}$$

Then, the bending moment and transverse shear force can be calculated from Eqs. (12) and (13).

5. Solutions of cracked FGM beams

Fig. 2b exhibits schematically the forced and free waves in the cracked FGM beam. Since a part of travelling waves are reflected at the crack location, the cracked FGM beam should be divided into three sub-beams at the driving source and crack location. For each sub-beam, the solutions of the transverse displacement and rotation can be expressed as

$$\begin{Bmatrix} W_i(x) \\ \Psi_i(x) \end{Bmatrix} = \begin{pmatrix} f_{1i} & f_{2i} & f_{3i} & f_{4i} \\ q_1 f_{1i} & -q_1 f_{2i} & -q_2 f_{3i} & q_2 f_{4i} \end{pmatrix} \{\chi\}, \tag{33}$$

where $\{\chi\} = \left\{ \mathrm{e}^{-k_1 x} \quad \mathrm{e}^{k_1 x} \quad \mathrm{e}^{-\mathrm{i}k_2 x} \quad \mathrm{e}^{\mathrm{i}k_2 x} \right\}^{\mathrm{T}}$; $i = 1, 2, 3$.

The transverse displacement, rotation, bending moment and transverse shear force at driving source x = 0 and crack location $x = L_1$ satisfy

$$W_1(0) = W_2(0), \quad \Psi_1(0) = \Psi_2(0), \quad M_1(0) = M_2(0), \quad Q_2(0) - Q_1(0) = F_0, \tag{34}$$

$$W_2(L_1) = W_3(L_1), \quad K_T\left[\Psi_3(L_1) - \Psi_2(L_1)\right] = M_3(L_1), \quad M_2(L_1) = M_3(L_1), \quad Q_2(L_1) = Q_3(L_1). \tag{35}$$

Because of the infinite length of sub-beam 1 and sub-beam 3, there is no reflect wave from the boundary of these two sub-beams. Hence, one can get $f_{11} = f_{31} = 0$ and $f_{23} = f_{43} = 0$. Then, the unknown vector can be defined by

$$\mathbf{f} = \left\{ f_{21} \quad f_{41} \quad f_{12} \quad f_{22} \quad f_{32} \quad f_{42} \quad f_{13} \quad f_{33} \right\}^{\mathrm{T}}. \tag{36}$$

Substituting $W_j(x)$ and $\Psi_j(x)$ into Eqs. (12) and (13), the bending moment and transverse shear force can be derived as

$$\begin{Bmatrix} M_j(x) \\ Q_j(x) \end{Bmatrix} = \begin{Bmatrix} D_{11} W_j'(x) \\ \kappa A_{55}\left[W_j'(x) + \Psi_j(x) \right] \end{Bmatrix} \tag{37}$$

where the prime symbol denotes the differential with respect to x.

Substituting Eqs. (33) and (37) into Eqs. (34) and (35), we have

$$\mathbf{C}_{\mathbf{oef}} \mathbf{f} = \mathbf{Q}, \tag{38}$$

where

$$\mathbf{Q} = \left\{ 0 \quad 0 \quad 0 \quad F_0 / \kappa A_{55} \quad 0 \quad 0 \quad 0 \quad 0 \right\}^{\mathrm{T}}, \tag{39}$$

$$\mathbf{C}_{\mathbf{oef}}=\begin{bmatrix} 1 & 1 & -1 & -1 & -1 & -1 & 0 & 0 \\ -q_1 & q_2 & -q_1 & q_1 & q_2 & -q_2 & 0 & 0 \\ -q_1k_1 & \mathrm{i}q_2k_2 & q_1k_1 & q_1k_1 & -q_2k_2 & -\mathrm{i}q_2k_2 & 0 & 0 \\ \Upsilon_2 & \Upsilon_1 & \Upsilon_2 & -\Upsilon_2 & \Upsilon_1 & -\Upsilon_1 & 0 & 0 \\ 0 & 0 & \mathrm{e}^{-k_1L_1} & \mathrm{e}^{k_1L_1} & \mathrm{e}^{-\mathrm{i}k_2L_1} & \mathrm{e}^{\mathrm{i}k_2L_1} & -\mathrm{e}^{-k_1L_1} & -\mathrm{e}^{-\mathrm{i}k_2L_1} \\ 0 & 0 & -q_1\mathrm{e}^{-k_1L_1} & q_1\mathrm{e}^{k_1L_1} & q_2\mathrm{e}^{-\mathrm{i}k_2L_1} & -q_2\mathrm{e}^{\mathrm{i}k_2L_1} & \Upsilon_3\mathrm{e}^{-k_1L_1} & -\Upsilon_4\mathrm{e}^{-\mathrm{i}k_2L_1} \\ 0 & 0 & -q_1k_1\mathrm{e}^{-k_1L_1} & -q_1k_1\mathrm{e}^{k_1L_1} & \mathrm{i}q_2k_2\mathrm{e}^{-\mathrm{i}k_2L_1} & \mathrm{i}q_2k_2\mathrm{e}^{\mathrm{i}k_2L_1} & q_1k_1\mathrm{e}^{-k_1L_1} & -\mathrm{i}q_2k_2\mathrm{e}^{-\mathrm{i}k_2L_1} \\ 0 & 0 & -\Upsilon_2\mathrm{e}^{-k_1L_1} & \Upsilon_2\mathrm{e}^{k_1L_1} & -\Upsilon_1\mathrm{e}^{-\mathrm{i}k_2L_1} & \Upsilon_1\mathrm{e}^{\mathrm{i}k_2L_1} & \Upsilon_2\mathrm{e}^{-k_1L_1} & \Upsilon_1\mathrm{e}^{-\mathrm{i}k_2L_1} \end{bmatrix}, \tag{40}$$

and $\Upsilon_1=\mathrm{i}k_2+q_2;\ \Upsilon_2=k_1-q_1;\ \Upsilon_3=q_1+\dfrac{D_{11}}{K_T}q_1k_1;\quad \Upsilon_4=q_2+\dfrac{D_{11}}{K_T}\mathrm{i}q_2k_2$. The unknowns can be obtained by solving Eq. (38).

6. Vibrational power flow analysis

The vibrational power flow combines both forces and velocities with the consideration of their phase angle. It is an important physical quantity in the analysis of the structural noise, vibration control, power transmission and source tracing. In the vibrational structure, it is necessary for vibrational energy analysis to study the time averaged value of energy injected into structures. For the harmonic force $F\mathrm{e}^{\mathrm{i}\omega t}$ and velocity response $V\mathrm{e}^{\mathrm{i}\omega t}$, the time-averaged power flow is defined by

$$P=\frac{1}{2}\mathrm{Re}(F\tilde{V})=\frac{1}{2}\left|F\right|^2\mathrm{Re}(\beta)=\frac{1}{2}\mathrm{Re}(-\mathrm{i}\omega F\tilde{Y}), \tag{41}$$

where F, Y and V are the complex number; Y is the displacement amplitude; Re and symbol (˜) denote the real part and complex conjugate of a complex number, respectively; $\beta=V/F$ is the force point mobility.

The input power flow can be expressed according to the power flowing into the beam at the excitation point $x = 0$

$$P_{in}=\frac{1}{2}\mathrm{Re}(-\mathrm{i}\omega F_0\tilde{W})\Big|_{x=0}. \tag{42}$$

For the FGM beam, the energy can be transmitted by the internal shear force and bending moment. Therefore, the transmitted power flow is expressed as

$$P_{tr}=\frac{1}{2}\mathrm{Re}(-\mathrm{i}\omega M\tilde{\Psi})+\frac{1}{2}\mathrm{Re}(-\mathrm{i}\omega Q\tilde{W}). \tag{43}$$

With the aid of Eq. (37), the transmitted power flow can be expressed in terms of the transverse displacement and rotation

$$P_{tr}=\frac{1}{2}\mathrm{Re}\left\{-\mathrm{i}\omega\left[D_{11}W'\tilde{\Psi}-\kappa A_{55}\left(W'+\Psi\right)\tilde{W}\right]\right\}. \tag{44}$$

Substituting the solutions of transverse displacement and rotation of intact and cracked FGM beams into Eq. (42) and Eq. (44), the input power flow and transmitted power flow can be determined.

7. Crack identification using continuous wavelet transform

The continuous wavelet transform (CWT) is widely applied in the damage identification of structures. CWT as a signal progressing method has the ability to identify the singularity in the input signal such as the static deflection, mode shape and dynamic response under a moving load. In our previous work [40], we proposed a new method for the crack identification of FGM beams by applying CWT to mode shapes. A new damage index is defined based on the position of the wavelet coefficient modulus maxima in the scale space. In this paper, this method is extended by applying CWT to the transmitted power flow distribution along the beam longitudinal direction. A brief introduction to this method is given as below.

According to the compatibility condition at the crack section, there is the discontinuity in transmitted power flow along the beam longitudinal direction. So, the spatial transmitted power flow $P_{tr}(x)$ can be treated as an input signal to be transformed by using CWT

$$Wf\left(b,s\right)=P_{tr}*\frac{1}{\sqrt{s}}\tilde{\varphi}\left(\frac{b}{s}\right)=P_{tr}*\tilde{\varphi}_{s}\left(b\right)=\int_{-\infty}^{+\infty}P_{tr}\left(x\right)\tilde{\varphi}_{b,s}\mathrm{d}x, \tag{45}$$

where $Wf(b,s)$ is the wavelet transform coefficient of $P_{tr}(x)$; the symbol $(*)$ denotes the convolution of two functions; b and s are the translation parameter and scale parameter to transform mother wavelet function $\varphi(x)$ to a series of wavelet function $\varphi_{b,s}=\frac{1}{\sqrt{s}}\varphi\left(\frac{x-b}{s}\right)$, respectively; and $\tilde{\varphi}(x)$ represents the complex conjugate of the wavelet function $\varphi(x)$ that satisfies [41]

$$\int_{-\infty}^{+\infty}\frac{\left|\hat{\varphi}\left(\varpi\right)\right|^{2}}{\left|\varpi\right|}\mathrm{d}\varpi=C_{\varphi}<+\infty, \tag{46}$$

where the wavelet function $\varphi(x)$ belongs to the Hilbert space of measurable, square-integrable one-dimensional functions $L^{2}(R)$; and $\hat{\varphi}(\varpi)$ is the Fourier transform of the wavelet function $\varphi(x)$. Eq. (46) implies $\varphi(x)$ with a zero average, i.e.,

$$\int_{-\infty}^{+\infty} \varphi(x)\mathrm{d}x = 0. \tag{47}$$

For the discontinuity in the spatial transmitted power flow, the Haar wavelet can be used as the mother wavelet function for the crack identification analysis. After applying CWT to the spatial transmitted power flow of the cracked FGM beam, the wavelet coefficients may exhibit the peak at the crack location and boundary. There are always peaks of the wavelet coefficient at the crack location when the scale parameter varies. In certain scale s_0 and spatial position b_0, $Wf(b_0, s_0)$ is associated with the maximal value of the wavelet coefficient if it satisfies

$$\frac{\partial Wf(b_0, s_0)}{\partial b} = 0 \quad . \tag{48}$$

According to the character of the wavelet coefficient maxima, a damage index (DI) is defined by [40]

$$DI(x) = \sum_{s=s_{\min}}^{s_{\max}} DWf,\ DWf = \begin{cases} 0 & , \dfrac{\partial Wf(x,s)}{\partial b} \neq 0, \\ 1 & , \dfrac{\partial Wf(x,s)}{\partial b} = 0, \end{cases} \tag{49}$$

where x denotes the distance of the detection point at the beam length direction from the driving source; $s_{\min}$ and $s_{\max}$ are the minimal and maximal scale parameter, respectively. The peak of DI indicates the position of the crack.

8. Numerical results and discussion

In this section, we first verify the present model and then discuss the input power flow, transmitted power flow and crack identification of cracked FGM beams. Unless otherwise stated, it is assumed that the cross section of beam is unit width and h = 0.1 m. The top surface of the FGM beam is made of pure aluminum. The material properties are Young's modulus $E_1 = 70$ GPa , mass density $\rho_1 = 2780\ \mathrm{kg/m^3}$ and Poisson's ratio $\mu = 0.33$. The amplitude of the driving force is taken as 100 N. The input power flow and the transmitted power flow are normalized as $10\log 10(P_{in} / F_0^2)$ (dB) and P_{tr} / P_{in}, respectively.

So far, we didn't find the literature on the power flow of the homogeneous and FGM cracked beam with the rectangular section. Therefore, it is difficult to compare the power flow of the cracked

homogeneous rectangular beam with the reported literature. So, we only compare the input power flow of an isotropic homogeneous intact beam to verify the present model. Fig. 3 shows the input power flow of an isotropic homogeneous beam with the circular cross section. The results given by Zhu et al. [29] are also plotted for comparison. The parameters of the homogeneous beam are taken as: radius $R = 0.025\text{m}$, mass density $\rho = 7800\text{kg/m}^3$, Young's modulus $E = 200\text{GPa}$ and Poisson ratio $\mu = 0.3$. It is observed that the present results are in good agreement with the results given by Zhu et al. [29].

8.1 Input power flow

Fig. 4 gives the effect of the Young's modulus ratio E_2 / E_1 on the input power flow of an intact FGM beam. The driving frequency varies from 1 Hz to 3000 Hz. It is found that the input power flow reduces with the increase of the driving frequency. The similar trend is also observed in the input power flow of homogeneous beams. For a given frequency, a greater Young's modulus ratio can lead to a smaller input power flow. Indeed, the Poisson's ratio must be varied along the thickness direction of the FGM beam in reality. Fig. 4 also adds the comparison of the input power flow for the FGM beams with the constant and varying Poisson's ratio. For the varying Poisson's ratio, it is assumed to change with the exponential function along the thickness direction. Clearly, we can observe that the effect of the Poisson's ratio is slight on the input power flow.

Fig. 5 illustrates the effect of the Young's modulus ratio E_2 / E_1 on the input power flow of cracked FGM beams with $a / h = 0.3$ and $L_1 / h = 20$. Unlike intact FGM beams, it is observed that the input power flows of cracked FGM beams produce the fluctuation with the variation of the frequency. The reason is that there is the reflection wave between the crack location and driving force position, which leads to the change of the transverse displacement at the driving force position $x = 0$, and in turn alters the characteristics of the input power flow at $x = 0$. Similar to the intact FGM beams, the input power flow of cracked FGM beams reduces as the frequency increases. Furthermore, for a given frequency, the input power flow of cracked FGM beams increases as the Young's modulus ratio increases.

Fig. 6 highlights the effect of the crack depth a / h on the input power flow of cracked FGM beams with $E_2 / E_1 = 5$ and $L_1 / h = 20$. The input power flow of cracked FGM beams fluctuates around the solid line that describes the input power flow of intact FGM beams. The fluctuation amplitude of the input

power flow curve is enlarged with the increase of the crack depth a/h. The fluctuation amplitude at low frequency is smaller than that at high frequency. Interestingly, we can see the intersections between the curves of cracked and intact FGM beams. It is indicated that the presence of cracks doesn't affect the input power flow at the intersections with special frequencies, such as ω = 90 Hz, 170 Hz, 280 Hz, 415 Hz, 575 Hz, 755 Hz, 995 Hz……. Furthermore, the variation of the crack depth has no effect on the wavelength of input power flow curves of cracked FGM beams.

The effect of the crack location L_1/h on the input power flow of cracked FGM beams with $a/h = 0.3$ and $E_2/E_1 = 5$ is shown in Fig. 7. The wavelength of the input power flow curve decreases as the location of the crack moves away from the driving force. For different crack locations, the input power flows have the same value at some special frequencies, such as 225Hz, 855 Hz, 1795 Hz and 2960 Hz.

Figs. 8-10 present the relationship between the input power flow and the crack location with various crack depths, Young's modulus ratios and driving frequencies, respectively. We can see that the input power flow of cracked FGM beams is a periodic function with respect to the crack location L_1/h. In Fig. 8 the amplitude of the input power flow increases as the crack depth increases. Clearly, the wavelength of the curves relating to the input power flow vs the crack location is not affected by the crack depth. In Fig. 9, the amplitude of the curves increases with the decrease of the Young's modulus ratio from 5 to 0.2. In Fig. 10, as the driving frequency increases, the amplitude of the curves increases and the wavelength of curves decreases.

8.2 Transmitted power flow

Fig. 11 shows the effect of the crack depth a/h on the transmitted power flow of cracked FGM beams with $E_2/E_1 = 5$ and $L_1/h = 10$. For an intact FGM beam, the transmitted power flow is kept as a constant value of 0.5. It means that the input power flow is transformed to the transmitted power flow that is divided into two equal parts propagating along the positive and the negative directions in the intact FGM beam. For a cracked FGM beam, the transmitted power flow curves fluctuate around the straight line of the intact FGM beam. The amplitude of the curves is enlarged with increasing crack depth. The crack depth does not influence the wavelength of the curves.

Fig. 12 exhibits the effect of the crack location L_1/h on the transmitted power flow of cracked FGM beams with $E_2/E_1=5$ and a/h=0.3. It is found that the amplitude of the fluctuation increases as the driving frequency increases from 1 Hz to 3000 Hz. Meanwhile, the wavelength of the curves reduces as the crack is further away from the driving force.

Fig. 13 shows the effect of the Young's modulus ratio E_2/E_1 on the transmitted power flow of cracked FGM beams with $a/h=0.3$ and $L_1/h=10$. It can be observed that the amplitude of the transmitted power flow curves become lager when decreasing the Young's modulus ratio from 5 to 0.2.

Figs. 14-16 show the relationship between the transmitted power flow and crack location for various Young's modulus ratios, crack depths and driving frequencies, respectively. Similar to the input power flow, the transmitted power flow is also a periodic function about the crack location. It is observed in Fig. 14 that the amplitude of the transmitted power flow curves increases with the decrease of the Young's modulus ratio. Fig. 15 reveals that the amplitude of the transmitted power flow curves increases as the crack depth increases. Fig. 16 shows that, as the driving frequency increases, the amplitude of the curves increases, while the wavelength of the curves decreases.

8.3 Crack identification

Fig. 17 gives the spatial distribution of the transmitted power flow of cracked FGM beams for various crack depth. It is seen that the transmitted power flow changes suddenly at the location of the crack. The sudden change is obvious for the large crack depth ($a/h=0.5$), while it is less significant for the small crack depth ($a/h=0.01$). This result indicates that the crack identification using the spatial distribution of the transmitted power flow is only effective for large crack depth.

Therefore, we need to explore a new method for the crack identification of FGM beams. This method should be effective for the FGM beam with both small and large crack depths. By applying the continuous wavelet transform (CWT) to the spatial distribution of the transmitted power flow, the new method developed in Section 7 is used for the crack identification of FGM beams. The damage index of the FGM beam is plotted in Fig. 18 for various crack depths with $E_2/E_1=5$, $\omega=1500$ Hz and $L_1/h=5$. It can be clearly seen that the damage index has a peak value at $x/h=5$ for both small and large crack depths. The peak indicates the location of crack where the wavelet coefficient modulus converges. Therefore, the

present wavelet-based crack identification method is effective for FGM beams even with a small crack depth.

9. Conclusions

This paper proposed the vibrational power flow analysis of cracked FGM beams with infinite length. The effect of the crack location, the crack depth and the Young's modulus ratio on the input power flow and transmitted power flow is discussed. A new crack identification method is developed by applying CWT to the transmitted power flow distribution along the beam longitudinal direction. It is found that:

1. Unlike intact FGM beams, the input power flow and transmitted power flow of cracked FGM beams produce the fluctuation with the variation of the frequency. The reason is that there is the reflection wave between the crack location and driving force position, which alters the characteristics of the power flow curves.
2. The amplitude of the power flow-frequency curves is increased with increasing crack depth. The crack depth does not influence the wavelength of the curves.
3. The input power flow and transmitted power flow of cracked FGM beams are a periodic function with respect to the crack location.
4. A new damage index is proposed for the crack identification of FGM beams by applying CWT to the spatial distribution of the transmitted power flow. This crack identification method is effective for FGM beams with both small and large crack depths.

Acknowledgements

The work described in this paper is supported by National Natural Science Foundation of China (Grant No. 11725207).

References

[1] R.H. Lyon, G. Maidanik, Power flow between linearly coupled oscillators, J. Acoust. Soc. Am. 34 (1962) 623–639.

[2] D.U. Noiseux, Measurement of Power Flow in Uniform Beams and Plates, J. Acoust. Soc. Am. 47 (1970) 238-247.

[3] G. Pavić, Measurement of structure borne wave intensity, Part I: Formulation of the methods, J. Sound Vib. 49 (1976) 221-230.

[4] H.G.D. Goyder, R.G. White, Vibrational power flow from machines into built-up structures, part I: Introduction and approximate analyses of beam and plate-like foundations, J. Sound Vib. 68 (1980) 59-75.

[5] H.G.D. Goyder, R.G. White, Vibrational power flow from machines into built-up structures, part II: Wave propagation and power flow in beam-stiffened plates, J. Sound Vib. 68 (1980) 77-96.

[6] H.G.D. Goyder, R.G. White, Vibrational power flow from machines into built-up structures, part III: Power flow through isolation systems, J. Sound Vib. 68 (1980) 97-117.

[7] O.M. Bouthier, R.J. Bernhard, Simple models of the energetics of transversely vibrating plates, J. Sound Vib. 182 (1995) 149-164.

[8] W. Zhang, H. Chen, D. Zhu, X. Kong, The thermal effects on high-frequency vibration of beams using energy flow analysis, J. Sound Vib. 333 (2014) 2588–2600.

[9] J.S. Chen, R.T. Wang, Wave propagation and power flow analysis of sandwich structures with internal absorbers, J. Vib. Acoust. 136 (2014) 041003-041003-8.

[10] J. Liu, W. He, D. Xie, Study on vibrational power flow propagation characteristics in a laminated composite cylindrical shell filled with fluid, Shock Vib. 2018(2018):1-19.

[11] X. Zheng, W. Dai, Y. Qiu, Z. Hao, Prediction and energy contribution analysis of interior noise in a high-speed train based on modified energy finite element analysis, Mech. Syst. Signal Pr. 126 (2019) 439–457.

[12] M. Sheng, T. Wang, M. Wang, X. Wang, X. Zhao, Effect of distributive mass of spring on power flow in engineering test, J. Sound Vib. 424 (2018) 365-377.

[13] L. Wang, T. Chen, Structural intensity analysis of the cantilevered plate under thermal load, Thin Wall. Struct. 139 (2019) 209–218.

[14] M. Koizumi, FGM activities in Japan, Compos. Part B-Eng. 28 (1997) 1-4.

[15] M. Naebe, K. Shirvanimoghaddam, Functionally graded materials: A review of fabrication and properties, Applied Materials Today 5 (2016) 223-245.

[16] S. Nikbakht, S. Kamarian, M. Shakeri, A review on optimization of composite structures Part II: Functionally graded materials, Compos. Struct. 214 (2019) 83-102.

[17] F. Xu, X. Zhang, H. Zhang, A review on functionally graded structures and materials for energy

absorption, Eng. Struct. 171 (2018) 309-325.

[18] C.M. Wang, L.L. Ke, A.N. Roy Chowdhury, J. Yang, S. Kitipornchai, D. Fernando, Critical examination of midplane and neutral plane formulations for vibration analysis of FGM beams, Eng. Struct. 130 (2017) 275–281.

[19] D.G. Zhang, Nonlinear bending analysis of FGM beams based on physical neutral surface and high order shear deformation theory, Compos. Struct. 100 (2013) 121–126.

[20] Y.L. Pei, P.S. Geng, L.X. Li, A modified higher-order theory for FG beams, Eur. J. Mech. A-Solid. 72 (2018) 186–197.

[21] M.A. Eltaher, A.E. Alshorbagy, F.F. Mahmoud, Determination of neutral axis position and its effect on natural frequencies of functionally graded macro/nanobeams, Compos. Struct. 99 (2013) 193–201.

[22] K. Larkin, A. Abdelkefi, Neutral axis modeling and effectiveness of functionally graded piezoelectric energy harvesters, Compos. Struct. 213 (2019) 25–36.

[23] S. Sahmani, B. Safaei, Nonlocal strain gradient nonlinear resonance of bi-directional functionally graded composite micro/nano-beams under periodic soft excitation, Thin Wall. Struct. 143 (2019) 106226.

[24] M. Rafiee, J. Yang, S. Kitipornchai, Large amplitude vibration of carbon nanotube reinforced functionally graded composite beams with piezoelectric layers, Compos. Struct. 96 (2013) 716–725.

[25] Y. Liu, D.W. Shu, Free vibration analysis of exponential functionally graded beams with a single delamination, Compos. Part B-Eng. 59 (2014) 166–172.

[26] ZH. Liu, JC. Niu, Vibrational energy flow model for functionally graded beams, Compos. Struct. 186 (2018) 17–28.

[27] T.Y. Li, W.H. Zhang, T.G. Liu, Vibrational power flow analysis of damaged beam structures, J. Sound Vib. 242 (2001) 59-68.

[28] T.Y. Li, T. Zhang, J.X. Liu, W.H. Zhang, Vibrational wave analysis of infinite damaged beams using structure-borne power flow, Appl. Acoust. 65 (2004) 91–100.

[29] X. Zhu, T.Y. Li, Y. Zhao, J.X. Liu, Structural power flow analysis of Timoshenko beam with an open crack, J. Sound Vib. 297 (2006) 215–226.

[30] X. Zhu, T.Y. Li, Y. Zhao, J. Yan, Vibrational power flow analysis of thin cylindrical shell with a circumferential surface crack, J. Sound Vib. 302 (2007) 332–349.

[31] T.Y. Li, X. Zhu, Y. Zhao, X.F. Hu, The wave propagation and vibrational energy flow characteristics

of a plate with a part-through surface crack, Int. J. Eng. Sci. 47 (2009) 1025–1037.

[32] A. Katunin, H. Lopes, J.V. Araújo dos Santos, Identification of multiple damage using modal rotation obtained with shearography and undecimated wavelet transform, Mech. Syst. Signal Pr. 116 (2019) 725–740.

[33] M. Rucka, K. Wilde, Crack identification using wavelets on experimental static deflection profiles, Eng. Struct. 28 (2006) 279-288.

[34] E. Douka, S. Loutridis, A. Trochidis, Crack identification in beams using wavelet analysis, Int. J. Solids Struct. 40 (2003) 3557-3569.

[35] X.Q. Zhu, S.S. Law, Wavelet-based crack identification of bridge beam from operational deflection time history, Int. J. Solids Struct. 43 (2006) 2299-2317.

[36] A.M. Parrany, Damage detection in circular cylindrical shells using active thermography and 2-D discrete wavelet analysis, Thin Wall. Struct. 136 (2019) 34–49.

[37] D. Broek, Elementary Engineering Fracture Mechanics, Martinus Nijhoff Publishers, Dordrecht, 1986.

[38] F. Erdogan, B.H. Wu, The surface crack problem for a plate with functionally graded properties, J. Appl. Mech. 64 (1997) 449-456.

[39] L.L. Ke, J. Yang, S. Kitipornchai, Y. Xiang, Flexural vibration and elastic buckling of a cracked Timoshenko beam made of functionally graded materials, Mech. Adv. Mater. Struct. 16 (2009) 488-502.

[40] L.F. Zhu, L.L. Ke, X.Q. Zhu, Y. Xiang, Y.S. Wang, Crack identification of functionally graded beams using continuous wavelet transform, Compos. Struct. 210 (2019) 473–485.

[41] S. Mallat, W.L. Hwang, Singularity detection and processing with wavelets, IEEE T. Informa. Theory 38 (1992) 617-643.

Figure captions

Fig. 1. A cracked FGM beam (a) and the massless rotational spring model connecting two sub-beams (b).

Fig. 2. The forced and free waves under the action of a harmonic force in an intact FGM beam (a) and a cracked FGM beam (b).

Fig. 3. The input power flow of intact circular FGM beam

Fig. 4. The effect of the Young's modulus ratio E_2 / E_1 on the input power flow versus frequency curves of intact FGM beams.

Fig. 5. The effect of the Young's modulus ratio E_2 / E_1 on the input power flow versus frequency curves of cracked FGM beams with $a / h = 0.3$ and $L_1 / h = 20$.

Fig. 6. The effect of the crack depth a / h on the input power flow versus frequency curves with $E_2 / E_1 = 5$ and $L_1 / h = 20$.

Fig. 7. The effect of the crack location L_1 / h on the input power flow versus frequency curves with $a / h = 0.3$ and $E_2 / E_1 = 5$.

Fig. 8. The effect of the crack depth a / h on the input power flow versus crack location curves with $E_2 / E_1 = 5$ and $\omega = 1500$ Hz.

Fig. 9. The effect of the Young's modulus ratio E_2 / E_1 on the input power flow versus crack location curves with $a / h = 0.3$ and $\omega = 1500$ Hz.

Fig. 10. The effect of the driving frequency ω on the input power flow versus crack location curves with $a / h = 0.3$ and $E_2 / E_1 = 5$.

Fig. 11. The effect of the crack depth a / h on the transmitted power flow versus frequency curves with $E_2 / E_1 = 5$ and $L_1 / h = 20$.

Fig. 12. The effect of the crack location L_1 / h on the transmitted power flow versus frequency curves with $E_2 / E_1 = 5$ and $a / h = 0.3$.

Fig. 13. The effect of the Young's modulus ratio E_2 / E_1 on the transmitted power flow versus

frequency curves with $E_2 / E_1 = 5$ and $a / h = 0.3$.

Fig. 14. The effect of the Young's modulus ratio E_2 / E_1 on the transmitted power flow versus crack location curves with $a / h = 0.3$ and $\omega = 1500$ Hz.

Fig. 15. The effect of the crack depth a / h on the transmitted power flow versus crack location curves with $E_2 / E_1 = 5$ and $\omega = 750$ Hz.

Fig. 16. The effect of the driving frequency ω on the transmitted power flow versus crack location curves with $a / h = 0.1$ and $E_2 / E_1 = 5$.

Fig. 17. The spatial distribution of the transmitted power flow of cracked FGM beams for various crack depth with $E_2 / E_1 = 5, \omega = 1500$ Hz and $L_1 / h = 5$.

Fig. 18. The Damage index of cracked FGM beams for various crack depth with $E_2 / E_1 = 5, \omega = 1500$ Hz and $L_1 / h = 5$.

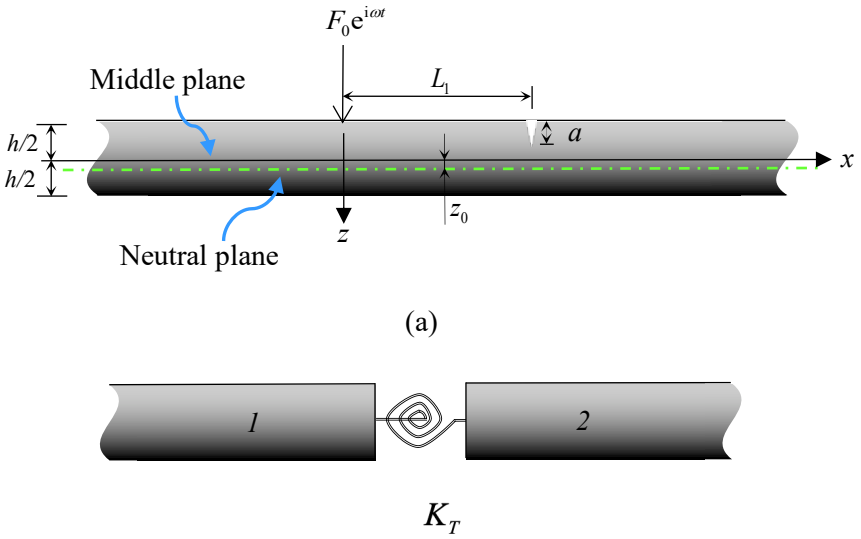

Fig. 1. A cracked FGM beam (a) and the massless rotational spring model connecting two sub-beams (b).

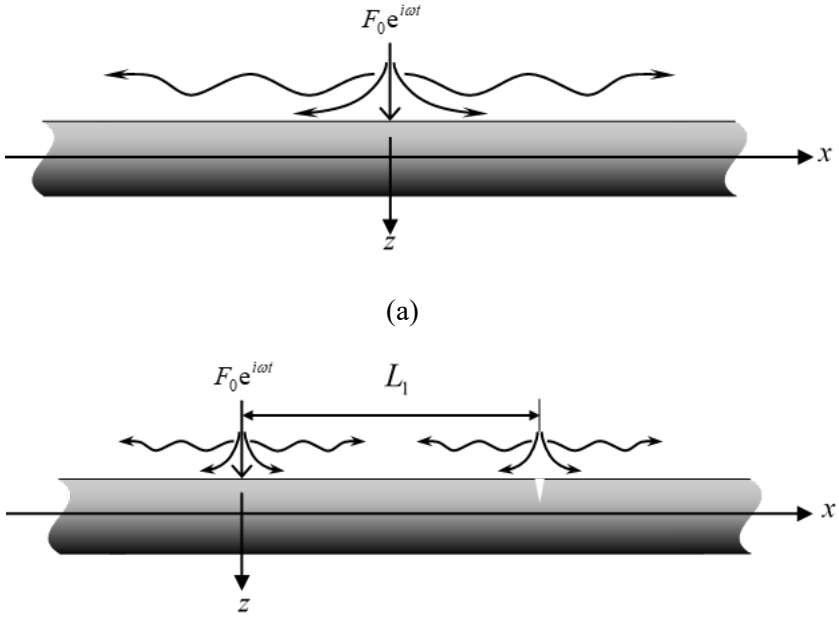

Fig. 2. The forced and free waves under the action of a harmonic force in an intact FGM beam (a) and a cracked FGM beam (b).

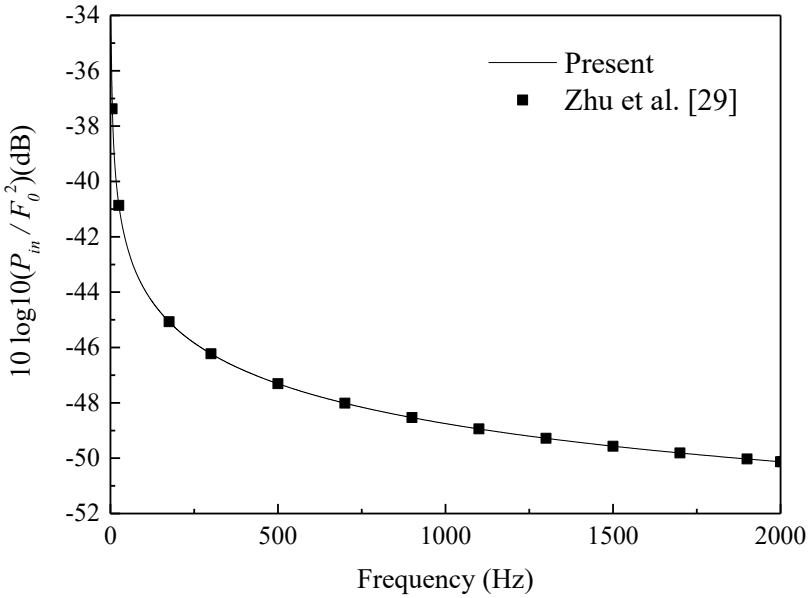

Fig. 3. The input power flow of an intact circular isotropic homogeneous beam

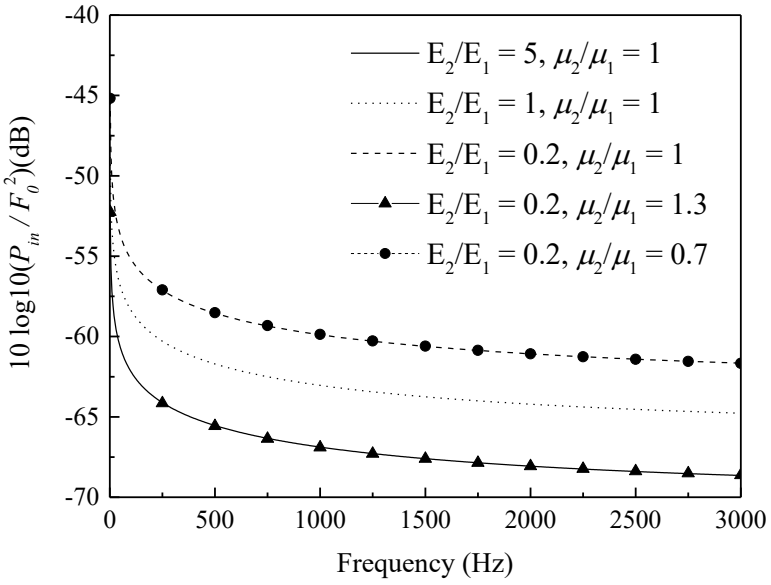

Fig. 4. The effect of the Young's modulus ratio E_2 / E_1 on the input power flow versus frequency curves of intact FGM beams.

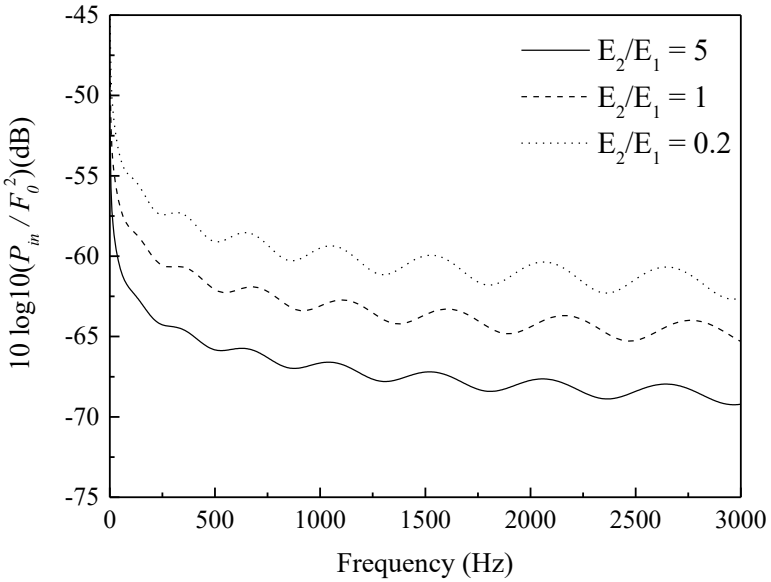

Fig. 5. The effect of the Young's modulus ratio E_2 / E_1 on the input power flow versus frequency curves of cracked FGM beams with $a / h = 0.3$ and $L_1 / h = 20$.

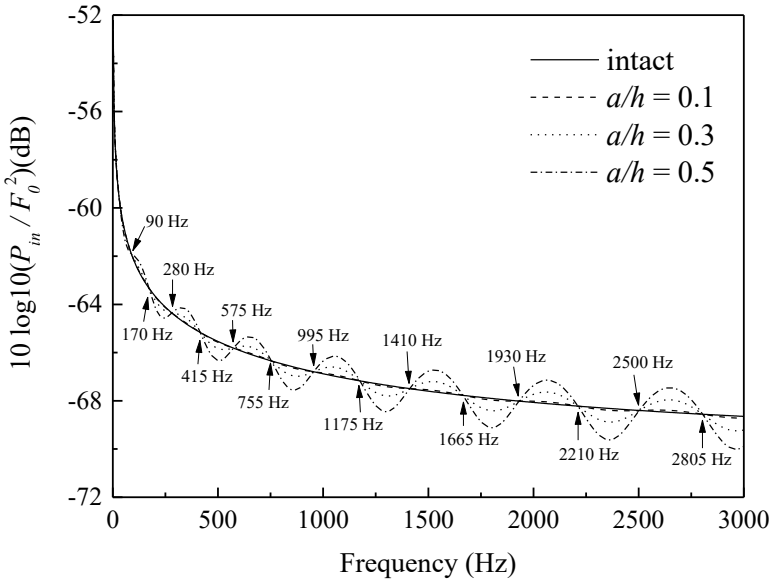

Fig. 6. The effect of the crack depth a/h on the input power flow versus frequency curves with $E_2/E_1 = 5$ and $L_1/h = 20$.

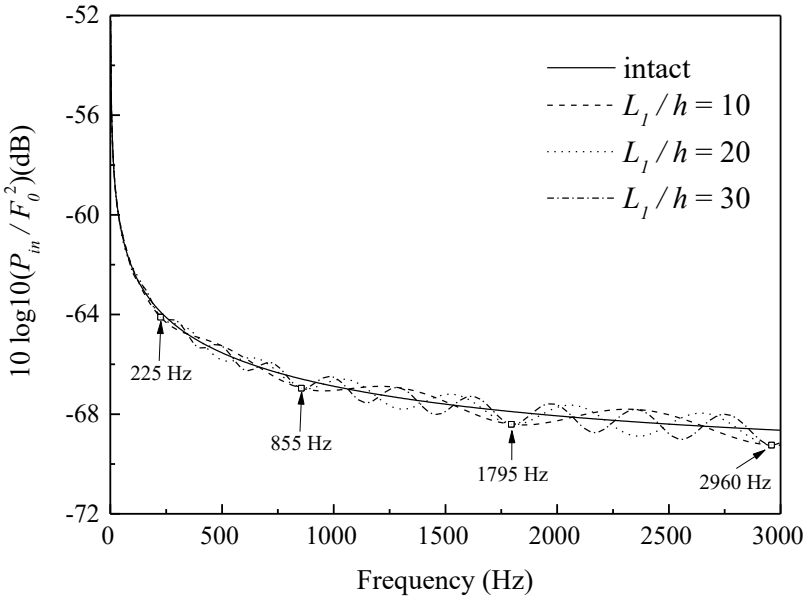

Fig. 7. The effect of the crack location L_1 / h on the input power flow versus frequency curves with $a / h = 0.3$ and $E_2 / E_1 = 5$.

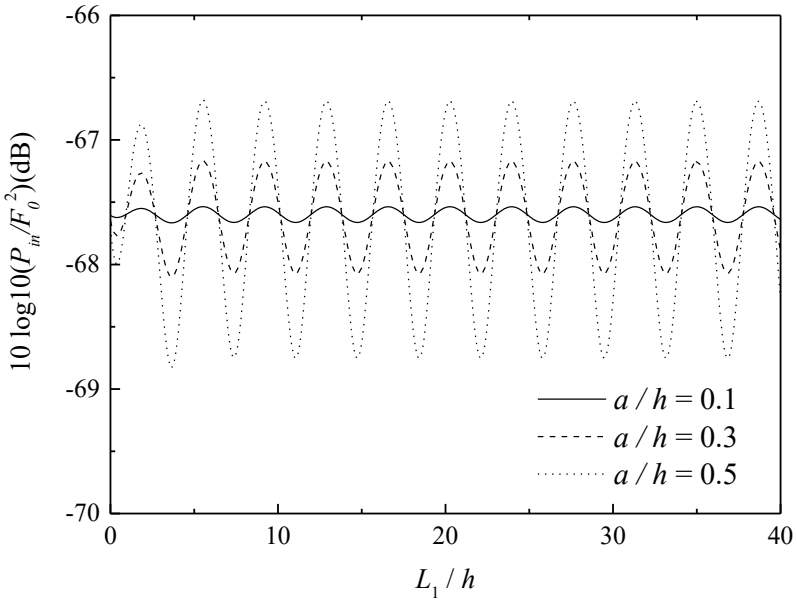

Fig. 8. The effect of the crack depth a / h on the input power flow versus crack location curves with $E_2 / E_1 = 5$ and $\omega = 1500$ Hz.

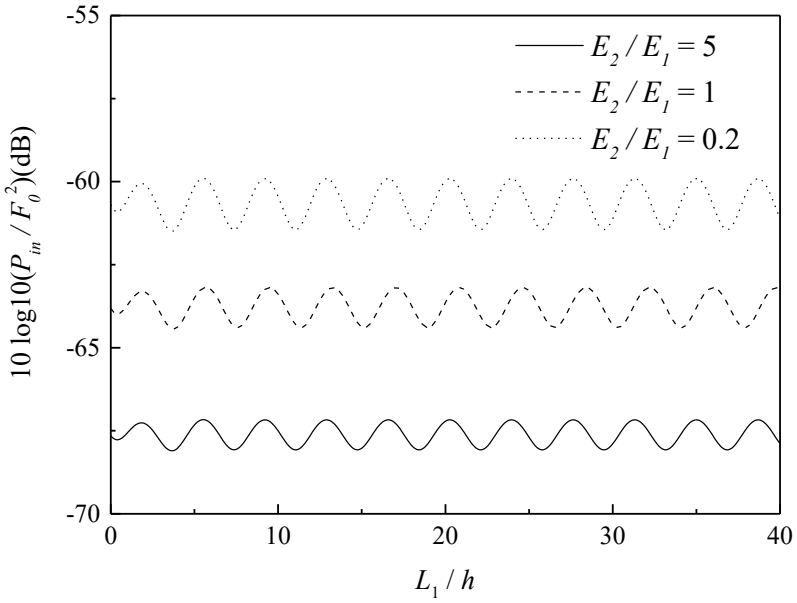

Fig. 9. The effect of the Young's modulus ratio E_2 / E_1 on the input power flow versus crack location curves with $a / h = 0.3$ and $\omega = 1500$ Hz.

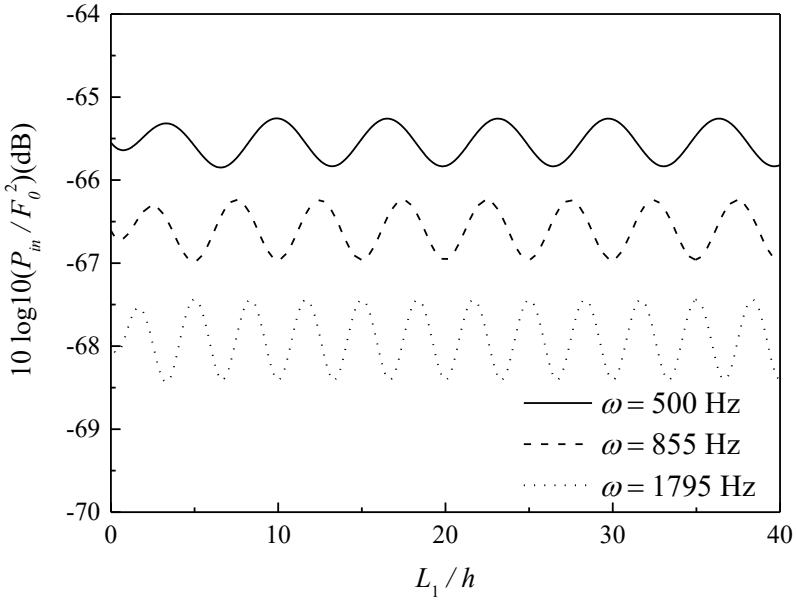

Fig. 10. The effect of the driving frequency ω on the input power flow versus crack location curves with $a/h = 0.3$ and $E_2/E_1 = 5$.

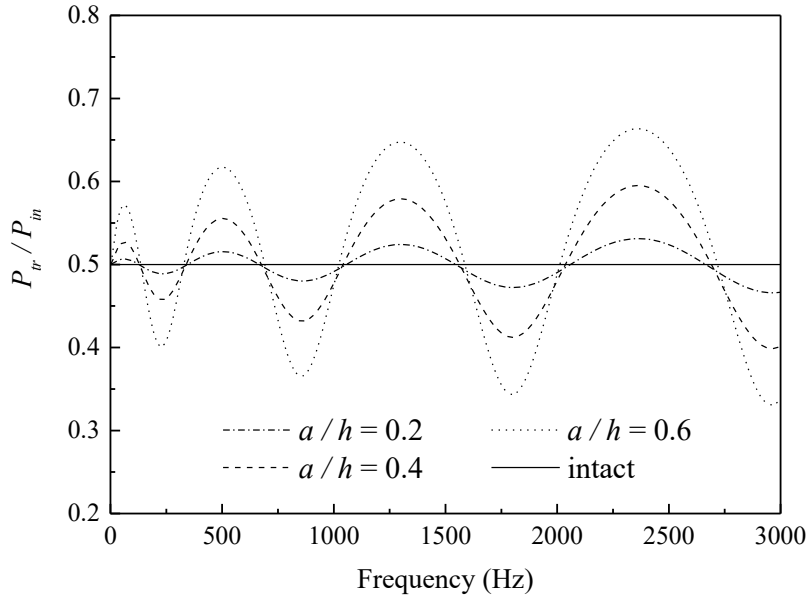

Fig. 11. The effect of the crack depth a / h on the transmitted power flow versus frequency curves with $E_2 / E_1 = 5$ and $L_1 / h = 20$.

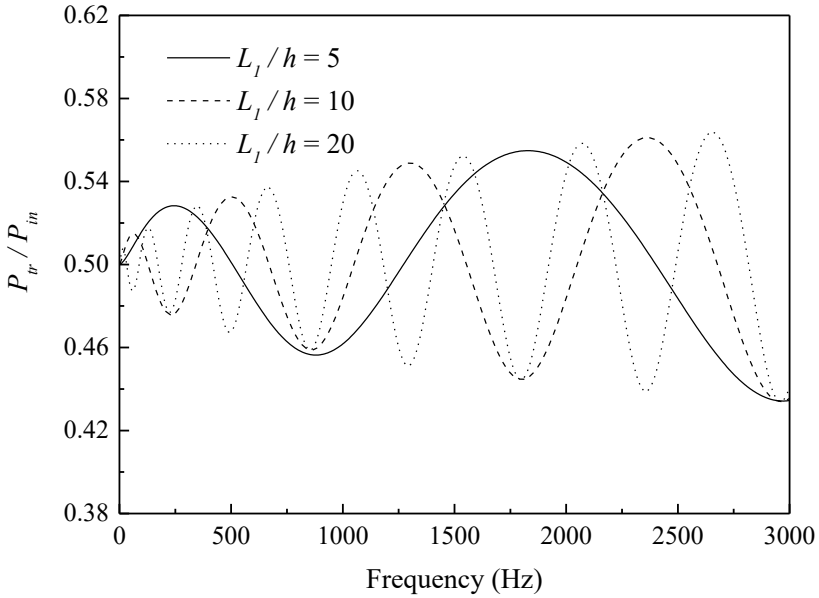

Fig. 12. The effect of the crack location L_1 / h on the transmitted power flow versus frequency curves with $E_2 / E_1 = 5$ and $a / h = 0.3$.

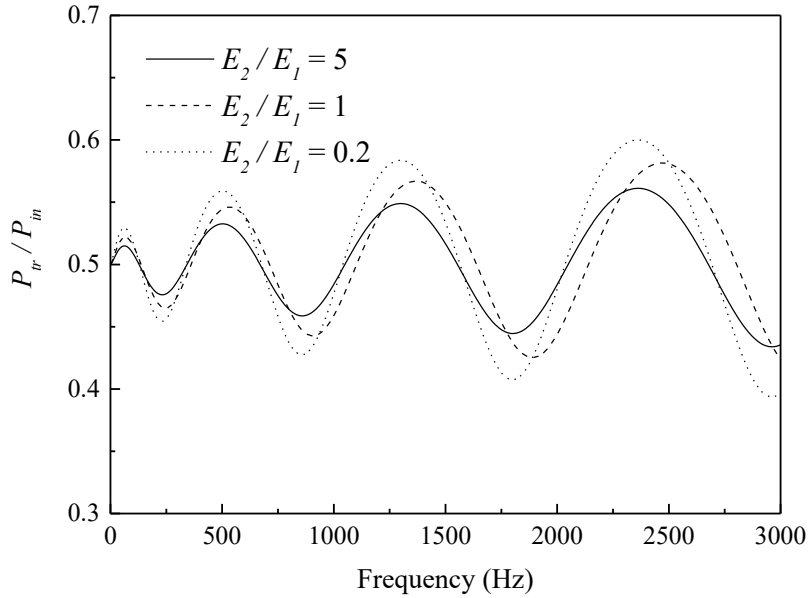

Fig. 13. The effect of the Young's modulus ratio E_2 / E_1 on the transmitted power flow versus frequency curves with $E_2 / E_1 = 5$ and $a / h = 0.3$.

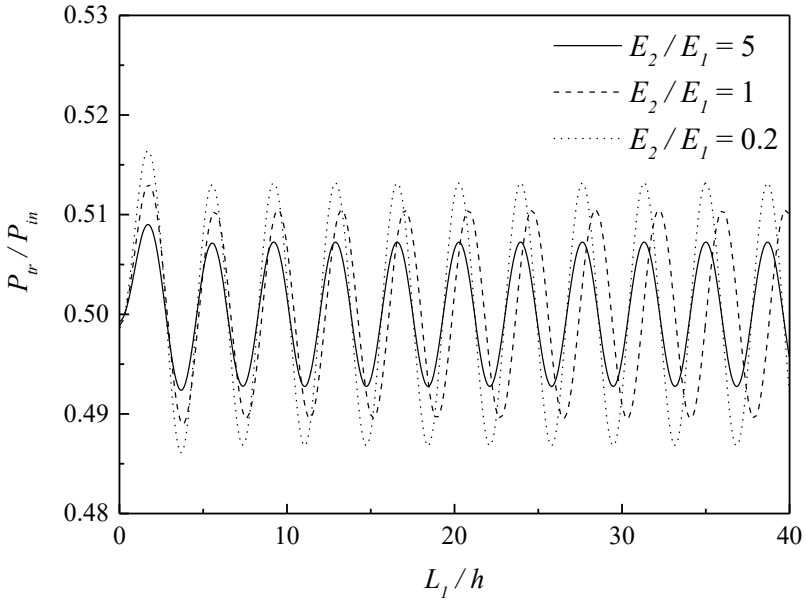

Fig. 14. The effect of the Young's modulus ratio E_2 / E_1 on the transmitted power flow versus crack location curves with $a / h = 0.3$ and $\omega = 1500$ Hz.

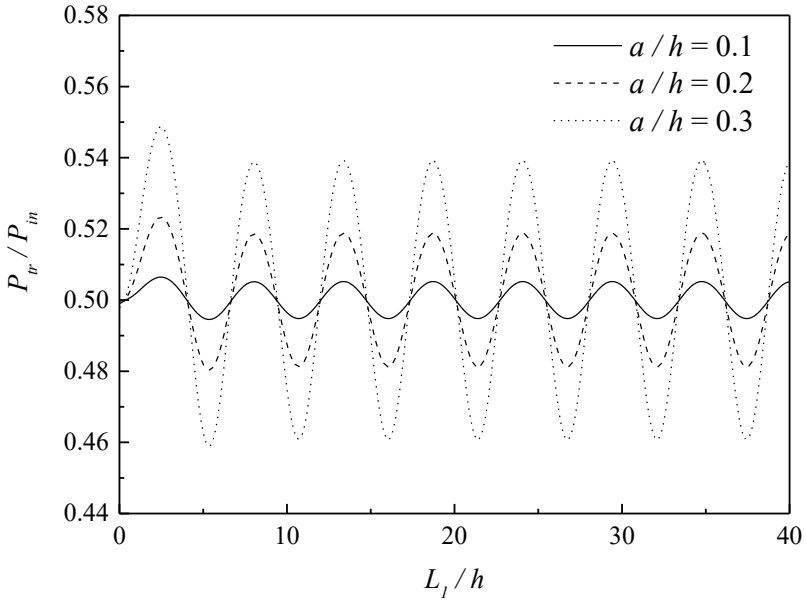

Fig. 15. The effect of the crack depth a / h on the transmitted power flow versus crack location curves with $E_2 / E_1 = 5$ and $\omega = 750$ Hz.

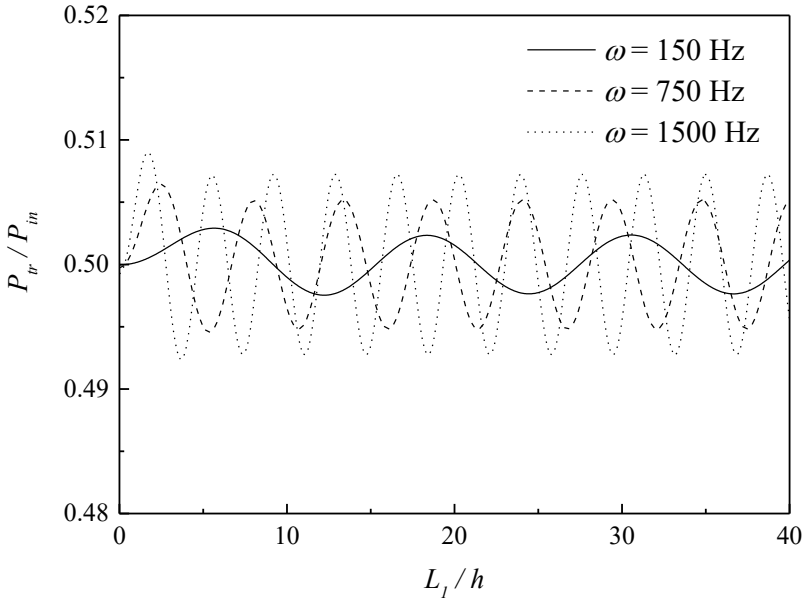

Fig. 16. The effect of the driving frequency ω on the transmitted power flow versus crack location curves with $a / h = 0.1$ and $E_2 / E_1 = 5$.

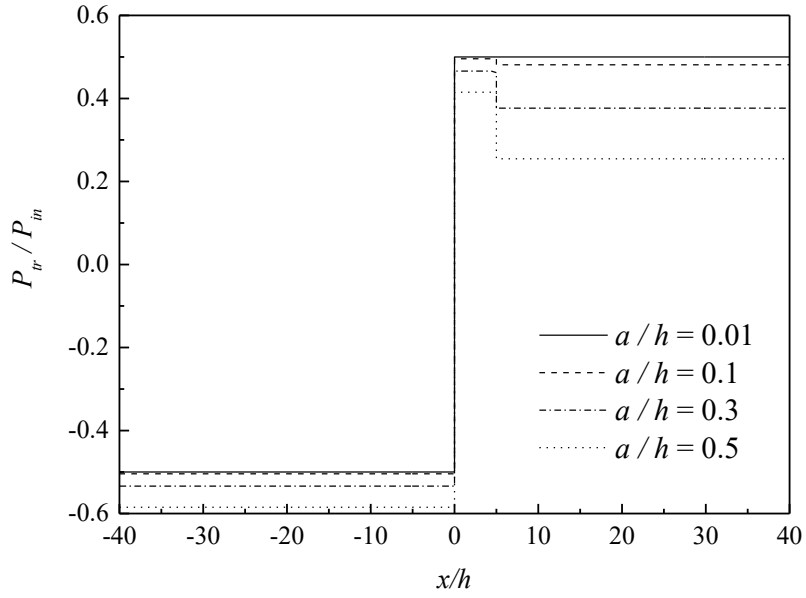

Fig. 17. The spatial distribution of the transmitted power flow of cracked FGM beams for various crack depth with $E_2 / E_1 = 5$, $\omega = 1500$ Hz and $L_1 / h = 5$.

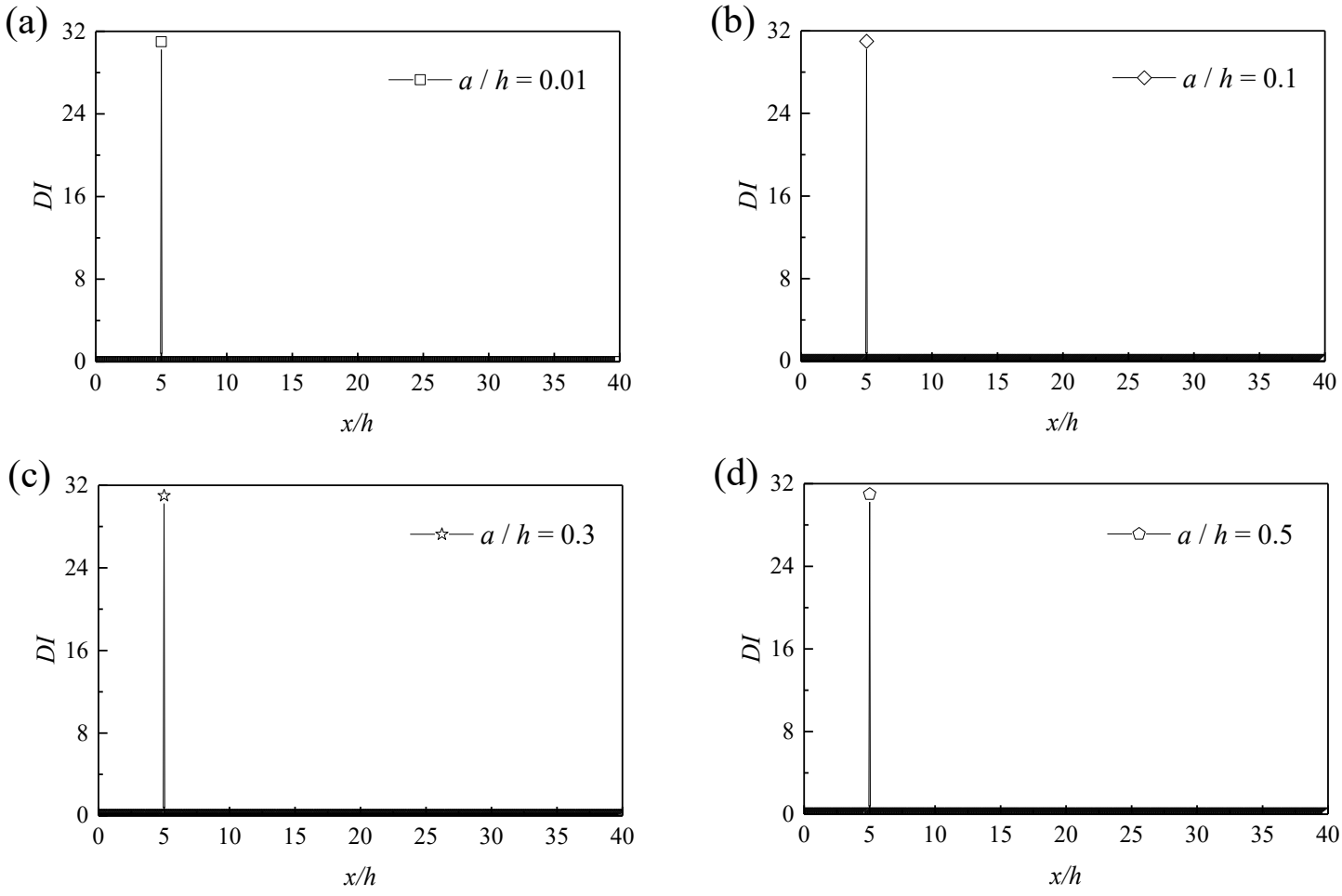

Fig. 18. The Damage index of cracked FGM beams for various crack depth with $E_2 / E_1 = 5$, $\omega = 1500$ Hz and $L_1 / h = 5$.